# Structure and bonding in photodiffused amorphous Ag-$GeSe_2$ thin films

A. Fischer-Colbrie* and A. Bienenstock
*Department of Materials Science and Engineering, Stanford University, Stanford, California 94305-2205*

P. H. Fuoss
*AT&T Bell Laboratories, Crawfords Corner Road, Holmdel, New Jersey 07733-1988*

Matthew A. Marcus
*AT&T Bell Laboratories, 600 Mountain Avenue, Murray Hill, New Jersey 07974-2070*
(Received 24 February 1988; revised manuscript received 10 August 1988)

Grazing-incidence x-ray scattering (GIXS) techniques have been used to study the local and intermediate-range order in photodiffused amorphous Ag-$GeSe_2$ thin films and a variety of Ag-Ge-Se alloys. Using synchrotron-radiation sources, the GIXS technique can be used in conjunction with radial-distribution-function analysis, differential anomalous x-ray scattering, and differential distribution-function analysis to study the structure of very thin amorphous films. With these techniques, we have determined that the local atomic structure of Ag-$GeSe_2$ films satisfies a model where Se—Ag dative bonds are formed, one Se—Ag covalent bond is formed for each Ag atom added (below a critical composition), and Ge—Ge bonds are created as Ag is added. This last result significantly modifies the intermediate-range order in this system.

## I. INTRODUCTION

The amorphous Ge-Se system undergoes unique changes in its optical, electrical, and chemical properties when irradiated by light, electrons, or ions.[1] One radiation-induced phenomenon in particular, the photodiffusion of Ag into evaporated or sputtered films of amorphous $GeSe_2$ ($a$-$GeSe_2$), is the subject of this paper. The photodiffusion process occurs when light with energy greater than the $GeSe_2$ semiconductor band gap is incident on a thin layer (100 Å) of Ag deposited onto an $a$-$GeSe_2$ film. Under those conditions, Ag rapidly diffuses into the $GeSe_2$ films.

The phenomenology of the photodiffusion of Ag into $a$-$GeSe_2$ is extremely well understood since it has been extensively characterized for use as a high-resolution photoresist and $e$-beam resist for the lithography of integrated circuits. Typically, a thin film of $a$-$GeSe_2$ is prepared and a Ag layer is either evaporated or deposited electrochemically in the form of $Ag_2Se$ ($\approx 100$ Å thick) onto its surface. In the presence of light, the Ag diffuses into the $a$-$GeSe_2$ with a very high diffusivity ($3\times10^{-14}$ $cm^2/s$) at room temperature.[2] (For $GeSe_2$ at room temperature, the ratio of the absolute temperature to the melting point, $T_m$, is 0.28.) Comparable diffusivities would be observed for thermal diffusion of Ge in $c$-Ge at $\approx 0.9T_m$, Ag into metallic Ag at $\approx 0.6T_m$, and Se diffusion into $c$-Se at $\approx 0.5T_m$.[3] The Ag concentration profile is Fickian and the diffusion depth into $a$-$GeSe_2$ after long exposure times (1–2 h) is about 1500 Å. However, the time dependence is too slow for a Fickian profile for reasons which are not understood.

As stated, photodiffusion occurs for photon energies greater than the semiconductor band bap of the chalcogenide substrate. The photodiffusion mechanism appears to be nonlocal since the light only penetrates several hundred Å. The diffusion process is also activated by electrons and ions, but the sensitivity and resulting properties are different for the various forms of irradiation.

With 4 at.% or greater mean Ag concentrations photodiffused into $a$-$GeSe_2$, the material is insoluble in strong bases, indicating that significant chemical changes occur with photodiffusion.

Chalcogenide glasses such as GeS, As-Se, and As-S also exhibit photoenhanced diffusion (including Cu photodiffusion to a much lesser extent), but the reaction kinetics and the apparent products are different. Photoenhanced diffusion has not been observed for the crystalline forms of these materials.

While the microscopic phenomenology of photodiffusion is well understood, little is known about the atomistic mechanisms or the specific structural aspects of the photodiffusion process. One difficulty in studying this system with direct structural x-ray techniques, which are well suited to the study of amorphous materials, is that Ag photodiffuses from the surface to a depth of only $\approx 1500$ Å, so that the measured signal from the film is both weak and overwhelmed by the scattering from the rest of the sample (including the substrate). In this work, we have used the grazing-incidence x-ray scattering (GIXS) approach developed for the study of structurally ordered interfaces[4] and surfaces[5] and adapted by us[6] for the study of amorphous films on substrates. Using synchrotron radiation, the GIXS technique can be used in conjunction with x-ray scattering and radial-distribution-function (RDF) analysis, differential anomalous x-ray scattering (DAS), and differential-distribution-function (DDF) analysis to study the structure of thin amorphous films.

 

This paper describes the structural study of very thin layers of Ag-$GeSe_2$ made by photodiffusion. GIXS measurements were performed on 250-Å- and 1500-Å-thick films of $a$-$GeSe_2$ (on single-crystal Si substrates) into which different amounts of Ag were photodiffused. Bulk (symmetric-Bragg) x-ray measurements at several wavelengths were also made of the bulk materials from which both RDF's and DDF's were obtained. In addition, Ag $K$-edge (fluorescence and transmission) EXAFS (extended x-ray-absorption fine-structure) measurements were performed on a select set of samples made by photodiffusion, sputtering, and melt quenching. These results are interpreted using previously proposed structural models for $a$-$GeSe_2$ (the starting material), $a$-(Ag-Ge-Se), and photodiffused (pd) Ag-$GeSe_2$. The goal of this work was to obtain insight into the atomic rearrangements brought about by the photodiffusion process.

This paper is divided into four sections. First, we describe current models of $a$-$GeSe_2$ and the photodiffusion process. Then, we discuss experimental techniques. Because of the developmental nature of the GIXS technique, descriptions of experimental and data-analysis methods are presented. The results of the GIXS, EXAFS, and anomalous scattering measurements are then presented. Finally, we discuss the implications of these results and propose a model for the structure of $a$-Ag-$GeSe_2$.

## II. Ag-Ge-Se STRUCTURAL MODELS

Since a broad compositional range of Ag-$GeSe_2$ can be made by photodiffusion, it is useful to consider the structure of $a$-$GeSe_2$ as an initial starting point in understanding the $a$-Ag-$GeSe_2$ structure. Two models have been proposed for $a$-$GeSe_2$. These have very similar local order but differ in the intermediate-range order. The first model is the chemically ordered covalent-random-network (COCRN) model, which consists of randomly bonded $GeSe_{4/2}$ tetrahedra linked to form a three-dimensional network.[7] This COCRN model is very similar to the $SiO_2$-network model. In the COCRN model, like-atom bonds (Ge—Ge and Se—Se) or phase separations (Ge- and Si-rich regions) are defects which, from entropy arguments, are statistically present.

In the second model, the raft model, proposed by Phillips,[8] the network also consists predominantly of $GeSe_{4/2}$ tetrahedra, but these units are covalently bonded together in layers having atomic arrangements which are similar to the layers of crystalline $GeSe_2$. A layer is composed of parallel chains of corner-sharing tetrahedra, cross-linked with pairs of edge-sharing tetrahedra. In the raft model, layers are terminated by Se-Se "dimers" parallel to the chains. From Mössbauer work, Boolchand *et al.*[9] suggest that the raft has six parallel chains (50–60 Å) rather than two. In both the model and the crystal, the layers are held together by van der Waals forces. In the raft model, like-atom bonds are a necessary part of the structure. In addition, since the rafts are Se rich, there is also a Ge-rich region. Phillips has suggested "ethanelike" chains of $Ge_2Se_{6/2}$ which are correlated with the Se-rich rafts. Thus, the material is phase separated and has two distinctive structures.

Little is known about the specific structural aspects of the photodiffused Ag-Ge-Se system. X-ray-photoelectron-spectroscopy (XPS) studies of the Ag, Se, and Ge $3d$ core levels suggest that the Ag interacts with Se but not with Ge in photodiffusion.[10] Optical spectra for $a$-$GeSe_2$ show that the excitation of Se lone-pair and bonding electrons can be resolved in $a$-$GeSe_2$, but not for samples into which 10% Ag has photodiffused.[11] These results suggest a rearrangement of the local structure via an interaction with Se.

A structural model for the photodiffusion of Ag into $a$-$GeSe_2$ was originally proposed by Phillips using the raft model.[8] In the presence of light, Ag reacts with the Se along the Se-rich edges of the stacks of rafts (regions of high strain energy and possibly some dangling bonds) forming channels of ion-conducting $Ag_2Se$. In one of its crystalline forms, bcc $Ag_2Se$ is a superionic conductor, with an ionic conductivity of 2 $\Omega^{-1}\,cm^{-1}$. In this picture, only the edges of the $GeSe_2$ layers are disturbed in the photodiffusion process, so that the center of the layer as well as interlayer correlations remain intact.

We know of no other detailed structural models for the photodiffusion of Ag into $a$-$GeSe_2$, but Kastner[12] has predicted that group-I metals (Cu,Ag,Au) in amorphous chalcogenide glasses will be fourfold coordinated by the chalcogenide. With its outer $s$ electron, the metal atom forms a covalent bond to the chalcogenide. Three other metal-chalcogenide bonds are formed datively (chalcogenide lone-pair electrons donated to the bond). The covalent and dative bonds cannot be distinguished because of resonance. The expected bond lengths are those of covalent bonds. The work of Hunter *et al.*[13] and of Laderman *et al.*,[14] who studied the local Cu environment in $a$-$As_2Se_3$ with (EXAFS), support this model.

## III. EXPERIMENT

### A. Sample preparation

The photodiffused Ag-$GeSe_2$ samples were prepared in three steps: (1) thermal evaporation of different thicknesses (250 and 1500 Å) of $a$-$GeSe_2$ onto single-crystal Si substrates; (2) thermal evaporation of different thicknesses of Ag (0–250 Å) onto the $GeSe_2$; (3) exposure to uv light to cause the Ag photodiffusion. The $GeSe_2$ evaporation source was made from 99.999%-pure Ge and Se materials, which were degassed, melted together, and homogenized at 800 °C for 2 d. Deposition rates were 10 Å/s for the $GeSe_2$ and 1 Å/s for the Ag. The base pressure was $3\times10^{-9}$ Torr and the operating pressure was $<10^{-6}$ Torr. The light source was an unfiltered 200-W Hg lamp and exposure time was $\approx$1 h to ensure complete diffusion of the Ag. During exposure, samples were cooled by forced air and remained cooler than $\approx$40 °C.

In addition to the photodiffusion samples, reference samples were prepared by two techniques. Sputtered films of different thicknesses of sputtered amorphous $GeSe_2$ and $Ag_{10}Ge_{30}Se_{60}$ were prepared using a single target to maintain composition uniformity. Melt-quenched samples of $a$-$GeSe_2$ and $Ag_{10}Ge_{36}Se_{54}$ (and other Ag-Ge-

Se compositions) were made by weighing appropriate proportions of the following chemicals: Ge (40-Ω ingot), Se (99.999%-pure shot), and $Ag_2Se$ (99.999%-pure lump) for a 3 g total weight (±0.000 03 g). The materials were placed into sorption-pumped ($\approx 10^{-4}$ Torr) quartz tubes, heated and rocked at 1050 °C for ≈12 h, and quenched into a saltwater ice bath. The quenched material was ground to a very fine powder in preparation for the x-ray experiment.

The samples' compositions and other parameters are summarized in Table I. The film thicknesses were determined by a quartz oscillator during the deposition process, and the Ag composition was determined by Rutherford backscattering (RBS). The Ge-Se composition was accurate to ≈1% based on extensive prior work with this evaporation system. Microprobe measurements for these samples were consistent with the preceding results, but the accuracy is limited by the thinness of the films.

### B. GIXS measurement technique and data analysis

Grazing-incidence x-ray scattering (GIXS) measurements were made of thin-film photodiffused and sputtered samples. Synchrotron radiation was used because it provides both the beam collimation necessary to obtain the depth sensitivity appropriate for the thin films as well as the intensity necessary for the weakly scattering noncrystalline films. In particular, focused wiggler beamlines IV-2 and VI-2 (8-pole, 18-kG and 54-pole, 8-kG magnets, respectively) were used during dedicated conditions (3 GeV, 50–100 mA) at the Stanford Synchrotron Radiation Laboratory (SSRL). In this section we discuss the GIXS measurements and analysis suitable for the study of amorphous materials. To obtain interpretable data, the weak diffuse scattering associated with amorphous films must be accurately measured over a large $2\theta$ angular range. A major complication is that, unlike in the crystalline case, it is not possible to simply determine background and substrate contributions. Hence, this analysis includes careful considerations of background and substrate contributions which, although minimized by the GIXS geometry, are still important.

A schematic of the GIXS configuration is shown in Fig. 1. The incident and scattered (determined by the detector position) beams are fixed at small angles ($\phi$ and $\phi'$) with respect to the sample surface. In the scattering measurement (intensity as a function of momentum transfer $k$) the detector is rotated about the axis normal to the sample surface (azimuthal angle $2\theta$). Thus, the scattering vector lies nearly parallel to the surface. In a symmetric scattering measurement, the substrate is rotated azimuthally in a coupled motion with the detector ($\theta$-$2\theta$ scans). After determining that these amorphous films showed cylindrical symmetry (unique axis normal to the surface), the substrate rotation ($\theta$) was eliminated for this work to maintain precise control of the incident angle. The diffractometer developed for this work is discussed by Fischer-Colbrie.[15]

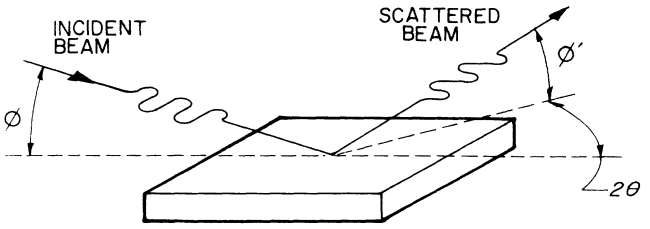


FIG. 1. Illustration of the grazing-incidence scattering geometry. During a $2\theta$-$\theta$ scan, the incident and takeoff angles $\phi$ and $\phi'$ are fixed while detector and sample rotate about sample surface normal. (For clarity, the reflected beam is not shown.)

TABLE I. List of the samples studied during the course of this work. See Sec. III A for a description of the sample-preparation techniques. ev denotes evaporation, pd photodiffusion, sp sputtering, and MQ melt quenching.

| Sample | Prep. method | Comp. | Thickness | Substrate |
|---|---|---|---|---|
| 1 | ev | $GeSe_2$ | 250 Å | Si(100) |
| 2 | ev and pd | $Ag_4Ge_{32}Se_{64}$ | 250 Å | Si(100) |
| 3 | pd | $Ag_4Ge_{32}Se_{64}$ | 1500 Å | Si(100) |
| 4 | pd | $Ag_{12}Ge_{29}Se_{59}$ | 250 Å | Si(100) |
| 5 | pd | $Ag_{25}Ge_{25}Se_{50}$ | 1500 Å | Si(100) |
| 6 | pd | $Ag_7Ge_{31}Se_{62}$ | 1500 Å | glass slide |
| 7 | sp | $Ag_{10}Ge_{30}Se_{60}$ | 1500 Å | Si(100) |
| 8 | sp | $Ag_{10}Ge_{30}Se_{60}$ | 7.5 μm | Kapton |
| 9 | MQ | $Ag_{10}Ge_{36}Se_{54}$ | bulk | |
| 10 | MQ | $GeSe_2$ | bulk | |

The advantage of this geometry is that the signal from the film can be isolated from the substrate signal by using refractive-index ($n < 1$ for x rays) and absorption effects.[16] By adjusting the grazing incident angle, the transmitted x rays can travel nearly parallel to the surface to be either scattered out or absorbed before reaching the substrate. For $a$-$GeSe_2$, using an x-ray energy of 11 keV, incident angles of 0.15°, 0.20°, and 0.25° yield a $1/e$ film penetration of 40, 170, and 2030 Å, respectively. This sensitivity of penetration depth to very small changes in incident angle means that the incident beam needs to be highly collimated and the samples need to be flat. For these measurements, the beam collimation was 0.13 mrad vertically and 2.0 mrad horizontally. To maintain sample flatness $\frac{1}{8}$-in.-thick polished single-crystal Si substrates were used. In practice, the incident angle was selected empirically by measuring the scattered intensity from the film as a function of incident angle, and then selecting an incident angle which maximized the signal from the film.

In general, the data collection included $k$-space measurements [$k = 4\pi \sin(\theta)/\lambda$, involving $2\theta$ motion], $k$-space fluorescence measurements to obtain an empirical correction for the variation of the amount of illuminated sample seen by the detector as a function of scattering angle [geometric correction $D(k)$], "background" scans ($k$-space scattering at very low incident angle), which were particularly useful for cases where there was a relatively strong low-$k$ signal (due to air or other parasitic scattering), and scans of incident angle for a fixed scattering vector, $k$, to aid in the selection of incident angle for the $k$-space measurements.

In quantitative analysis of GIXS data, the structure-

dependent scattering normalized to a per-atom scattering strength is desired. In the usual manner for amorphous materials,[17,18] $I_f(k)$, the signal from the amorphous film, can be separated into this structure-dependent term, $i_f(k)$, a structure-independent (self-atom) elastic scattering term, $I_{f,\mathrm{ind}}(k)$, and an inelastic scattering term, $I_{f,\mathrm{inc}}(k)$,

$$I_f(k)=i_f(k)+I_{f,\mathrm{ind}}(k)+I_{f,\mathrm{inc}}(k) . \quad (1)$$

The second and third terms in Eq. (2) are functions of composition, the complex scattering factors, and the incoherent scattering, only. Thus, they can be calculated explicitly. In this work, the values for the scattering factors and incoherent scattering are obtained from parametric fits by Cromer and Mann[19] and Balyuzi,[20] respectively. The anomalous scattering factors are obtained from Cromer and Liberman.[21]

The normalized scattering, $I_f(k)$, is obtained from the experimental data using methods described by Fuoss,[17] with modifications arising from the GIXS geometry. In particular, corrections are necessary for the polarization, $P(k)$, as well as variations in the amount of sample seen by the detector, $D(k)$. In these experiments, it was also necessary to account for finite penetration of the beam into the substrate as well as ($k$-independent) film and substrate absorption, $A_f$ and $A_s$. The measured signal, $I_m$, scaled by the normalization constant $K$, is given by

$$KI_m(k)=I_f(k)A_fP(k)D(k) + I_s(k)A_sP(k)D(k)+I_bD(k) , \quad (2)$$

where $I_f$ and $I_s$ are the scattering from the film and substrate, respectively, and $I_b$ is a $k$-independent background signal due to parasitic sattering and/or fluorescence.

The polarization correction depends on the experimental parameters $2\theta$ and $f'$, as well as the fractions of the incident beam which are horizontally, $h$, and vertically, $v$ ($=1-h$), polarized according to

$$P(h,2\theta,\phi')\approx h\cos^2(2\theta)+v\cos^2(\phi') \quad (3)$$

where the incident angle is small. Because of the large value of $h$ ($\approx 0.96$) for this synchrotron-radiation experiment,[22,15] the first term dominates and there is a deep minimum in the scattered intensity when the detector is near $2\theta=90°$. For the 11-keV x-ray-energy data, this minimum occurs at $k=7.9$ Å$^{-1}$.

The absorption corrections depend on the composition, density, and thickness of the film and substrate, $\phi$ and $\phi'$, and can be calculated. For the film, the correction is given by

$$A_f=\left[\frac{\rho_{0,f}A_0D_f(\phi)\sin(\phi')}{\sin(\phi)[\sin(\phi')-\mu_fD_f(\phi)]}\right] \times(1-\exp\{-t[1/D_f(\phi)+\mu_f/\sin(\phi')]\}) , \quad (4)$$

where $\rho_{0,f}$ is the average density of the film, $A_0$ is the (illuminated) sample area, $D_f(f)$ is the film $1/e$ penenetration depth at shallow incident angles, $t$ is the film thickness, and $\mu_f$ is the linear absorption coefficient of the film.

Analogous expressions can be written for the substrate scattering, $I_s$, and for corrections to the substrate scattering. It is important to note that the substrate is effectively infinitely thick. In this work we assume that the only signal observed in this geometry from the single-crystal Si substrate is the inelastic scattering.

To accurately correct for geometric aberations in the GIXS geometry, the detection linearity, $D(k)$, is needed. $D(k)$ was obtained from measurement of the sample's Ge $K\alpha$ fluorescence as a function of $2\theta$ with the x-ray energy slightly above the Ge $K$-absorption edge. In the analysis of the GIXS data, the measured signal is divided by a polynomial spline fit to $D(k)$. As in the case of the polarization function, the detector linearity function has a minimum near $2\theta=90°$, where the detector sees the smallest illuminated area of the sample.

In the normalization of the GIXS data, it is evident that large corrections to a weak signal must be made in the region near $2\theta=90°$. These corrections also exaggerate noise, which adds uncertainty to the analysis. In spite of this difficulty, the horizontally oriented sample (and scattering plane) is preferred over the vertically oriented sample with smaller polarization correction, because the horizontal sample subtends a much larger fraction of the incident beam (due to the spatial and divergent characteristics of the synchrotron beam) and yields an estimated factor-of-20 increase in signal. The next generation of high-brightness synchrotron-radiation sources will allow a vertical sample orientation to be used.

In the RDF analyses of this work, the structure-dependent normalized data were divided by Warren's approximation for the square of the average scattering factor before applying the Fourier sine transform. In a multicomponent system, this factor is given by[18]

$$\langle f^2(k)\rangle=\left[\sum_\alpha X_\alpha[(f_{\alpha,0}+f'_\alpha)^2+(f''_\alpha)^2]^{1/2}\right]^2 , \quad (5)$$

where $f_{\alpha,0}$, $f'_\alpha$ and $f''_\alpha$ are the atomic-scattering factors with real and imaginary corrections, respectively, and the sum over $\alpha$ is over the different elements in the system. The resulting RDF peak areas represent the average number of "average" atoms around an average central atom.

### C. Differential anomalous scattering measurements and analysis

Ge, Se, and Ag $K$-edge DAS measurements, discussed below, were made on bulk melt-quenched (MQ) $GeSe_2$ and MQ $Ag_{10}Ge_{36}Se_{54}$. Transmission DAS Ag $K$-edge measurements were made on $Ag_{10}Ge_{30}Se_{60}$ sputtered onto Kapton films. GIXS Ge $K$-edge DAS measurements were made of a 1500-Å-thick film of $GeSe_2$ evaporated onto a Si substrate.

The DAS methods used in this work are described by Fuoss.[17] These involve the differences between scattering

measurements taken at two different photon energies below the $K$-absorption edge of one of the elements, one energy far below the edge ($-1000$ eV) and one closer to the edge ($-14$ eV). In particular, for a binary $a$-$b$ system, the difference of two normalized structure-dependent scattering curves [$i(k,E_1)$ and $i(k,E_2)$] yield the differential structure function (DSF). The DSF weighted by the structure-dependent weighting function, $W(k,E_1,E_2)$ can be Fourier transformed to yield the DDF according to

$$\frac{2r}{\pi}\int \frac{i(k,E_1)-i(k,E_2)}{X_a(f'_{a1}-f'_{a2})\{F[2f_{a,0}(k)+f'_{a1}+f'_{a2}]+2(1-F)[f_{b,0}(k)+f'_{b1}]\}}k\sin(kr)dk+4\pi r^2(\rho_{a,0}+\rho_{b,0})$$
$$=4\pi r^2\frac{(2f_{a,0}+f'_{a1}+f'_{a2})\rho_{aa}+2(f_{b,0}+f'_{b,1})\rho_{ab}+\rho_{a,0}[1-(2f_{a,0}+f'_{a1}+f'_{a2})]+\rho_{b,0}[1-2(f_{b,0}+f'_{b1})]}{F(2Z_a+f'_{a1}+f'_{a2})+2(1-F)[Z_b(k)+f'_{b1}]}, \quad (6)$$

where both energies are below the absorption edge of element $a$, $f_{a,0}, f'_{a,1}, f'_{a,2}$ are the atomic scattering factor and real corrections at the two energies $E_1$ and $E_2$, respectively, $f_{b,0}$ and $f'_{b,1}$ are the atomic scattering factor and real correction to element $b$ (assumed not to change at the two energies), $F$ is the ratio of $a$—$a$ bonds to $a$—$a$ plus $a$—$b$ bonds (for the shell of interest) and $1-F$ is the ratio of $a$—$b$ bonds (when $F=0$, the material is chemically ordered and when $F=X_a$ it is randomly ordered), $\rho_{a,0}$ and $\rho_{b,0}$ are the average atomic densities of element $a$ and $b$, respectively, and $\rho_{aa}$ and $\rho_{ab}$ are the radial density of $a$ and $b$ atoms, respectively, around $a$. The areas under the peaks of this function yields the average number of atoms around element $a$, within the volumes of those peaks.

### D. EXAFS measurements and analysis

Transmission EXAFS experiments were performed on melt-quenched $Ag_{10}Ge_{36}Se_{54}$ glass, sputtered- (sp-) $Ag_{10}Ge_{30}Se_{60}$, and crystalline- ($c$-) $Ag_2Se$. The first two samples are from the same material studied in the x-ray-scattering measurements discussed earlier. Fluorescence EXAFS measurements were made on 1500-Å-thick pd $Ag_7Ge_{31}Se_{62}$ films deposited onto 75-$\mu$m-thick glass slides. Four of these samples were stacked together, in order to obtain measurable signal from the films. A Lytle fluorescence detector (sealed ion chamber),[23] with a 75-$\mu$m-thick Pd filter, filled with Kr was used to detect the fluorescence signal. In both the transmission and fluorescence EXAFS measurements, the samples were cooled to liquid-nitrogen temperature. The data were collected at the Stanford Synchrotron Radiation Laboratory (dedicated 3 GeV and 50–100 mA) on an 8-pole wiggler (17 kG) side station (Branchline 4-3). Si(220) monochromator crystals (detuned to accept 90% of the incident beam) provided an energy resolution of 7 eV at the Ag K edge (25.5 keV).

EXAFS curve-fitting[24,25] and Fourier-transform[26] methods were used to analyze these data. The relatively well-defined first-neighbor shell in the glasses suggested by Fourier-transform methods support the reliability of curve-fitting methods. Theoretical values for the back-scattering amplitude and total phase shifts calculated by Teo and Lee[24] were used because of the lack of suitable reference compounds. (The Ag—Se bond type in $c$-$Ag_2Se$ appears to be quite different from that of the amorphous materials.)

Typical calculations for the accuracy of the distances obtained in EXAFS is 0.01 Å.[25] However, this value depends on the shape of the distribution of the nearest neighbors. For an asymmetric distribution, the EXAFS is heavily weighted by the shortest distances. Our analysis assumes that the absolute values of the distances obtained are not accurate, but the relative distances are significant.

## IV. RESULTS

In this section the GIXS results obtained for Ag-$GeSe_2$ films made by photodiffusion are discussed and compared to bulk Ag-Ge-Se glasses made by quenching from the melt (MQ) and by sputtering (sp). This comparison includes RDF analyses as well as a DDF analysis of MQ Ag-Ge-Se. The section concludes with a presentation of the Ag-edge EXAFS results.

### A. GIXS results for photodiffused Ag-$GeSe_2$

The x-ray-scattering patterns for $a$-$GeSe_2$ films, into which Ag has been photodiffused, are shown in Fig. 2. The Ag concentrations are 0, 4, 12, and $\approx$25 at. %. The first three samples are 250 Å thick, while the most Ag rich is 1500 Å thick. In the figure the four curves have been scaled to constant intensity of the largest peak ($k=2$ Å$^{-1}$). As discussed earlier, the minimum in the scattered intensity near $k=7.9$ Å$^{-1}$ is due to the highly horizontally polarized synchrotron radiation as well as the detector function (sample area), both of whose effects are greatest when the detector is at $2\theta=90°$.

The primary difference between these curves is the reduction in intensity of the low-$k$ ($\approx 1$ Å$^{-1}$) peak, from a strong peak for pure $GeSe_2$ to no peak for $\approx$25 at. % Ag. With the addition of 25 at. % Ag, there is also a merging of the second and third peaks as well as an increase in the small-angle scattering (SAXS). These results indicate that large changes in the structure take place with photodiffusion.

As shown by Fuoss *et al.*,[27] the first peak in $a$-$GeSe_2$ is due to Ge-Ge correlations. Our quasicrystalline (qc) modeling work[6,15] suggests that the low-$k$ peak arises from chemically ordered corner- and edge-sharing $GeSe_{4/2}$ tetrahedra (including contributions from both inter- and intralayer correlations). The disappearance of

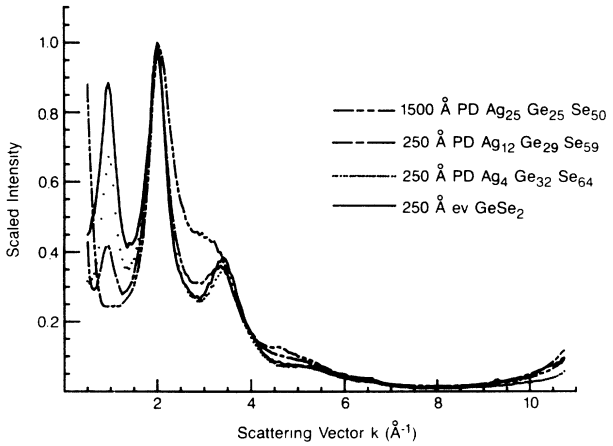


FIG. 2. GIS patterns (scaled to peak intensity of 1) for Ag-Ge-Se films made by photodiffusion (pd) of different amounts of Ag (0, 4, 12, and 25 at.%) into evaporated $GeSe_2$ films. $E_{photon} = 11$ keV.

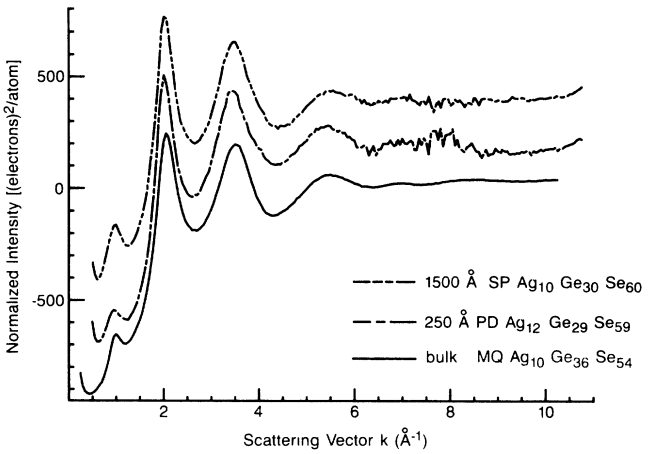


FIG. 3. Structure-dependent normalized scattered intensity for *a*-Ag-Ge-Se materials of comparable Ag concentration (10 at.%) made by photodiffusion (pd), sputtering (sp), and melt quench (MQ). The curves are offset 200, 400, and 0 $e^2$/atom, with respect to the preceding list. Films measured in GIS geometry and bulk samples measured in symmetric Bragg geometry.

this peak with the addition of Ag indicates changes in this intermediate-range order.

None of our scattering data show evidence of crystallinity, which would appear as sharp diffraction peaks. The small bumps which appear at 6.5 Å$^{-1}$ for the 250 Å evaporated $GeSe_2$ and at 9.25 Å$^{-1}$ for the 1500-Å-thick photodiffused $Ag_{25}Ge_{25}Se_{50}$ sample can be indexed as the Si(440) and Si(800) substrate peaks, respectively, and disappear for other substrate rotations $\theta$.

Small-angle scattering is not observed with either the 0- or 4-at.% Ag samples, but is evident for the 12-at.% sample and is still stronger for the 25-at.% Ag sample. The increase in the SAXS with the addition of Ag suggests that inhomogeneities are introduced by the photodiffusion of Ag. These inhomogeneities are probably a phase separation created by the photodiffusion reaction, since SAXS is not present in the *a*-$GeSe_2$ sample. (We have performed an extensive search for SAXS in *a*-$GeSe_2$. This search included measurements near the Ge *K*-absorption edge, where anomalous scattering effects would maximize the contrast between Ge-rich and Se-rich regions. Those results will be presented in a separate paper.)

### B. Comparison of pd Ag-GeSe$_2$ to other Ag-Ge-Se glasses

In Fig. 3 normalized structure-dependent intensity data, $i_f(k)$, for the 250-Å-thick, 12-at.% Ag photodiffused film are compared to samples of comparable Ag concentration made with other preparation methods: a 1500-Å-thick sputtered $Ag_{10}Ge_{30}Se_{60}$ film and a MQ (bulk) sample of $Ag_{10}Ge_{36}Se_{54}$. The normalization parameters are listed in Table II.

The curves for the three glasses are qualitatively quite similar. The curves differ primarily in the heights of the first two peaks and, to a much lesser degree, in peak positions. Whether these differences are due to a real structural effect or normalization error is difficult to determine since the overall shape of the curve over the full $k$ range is sensitive to normalization parameters as well as small background contributions.

### C. RDF's of *a*-Ag-Ge-Se

Figure 4 shows the RDF's for the photodiffused samples of Fig. 1. Table III summarizes the peak positions [determined from $r(\rho(r)-\rho_0)$] and areas [from $4\pi r^2\rho(r)$]. The increase in near-neighbor separation (2.37–2.62 Å) with increasing Ag concentration is expected since Ag-(Ge,Se, or Ag) distances in crystalline $Ag_2Se$ (Refs. 28–32) or $Ag_8GeSe_6$ (Ref. 33) (2.45–2.85 Å) tend to be larger than Ge-Se (Ref. 34) (2.37 Å), Ge-Ge (Ref. 35) (2.45 Å), or Se-Se (Ref. 35) (2.34 Å). The first peak area rises from $\approx 2.5$ to 3.3 average atoms and is significantly broadened with increasing Ag concentration. Overall, the RDF becomes a much smoother function. That is, the local structure approaches the average density very

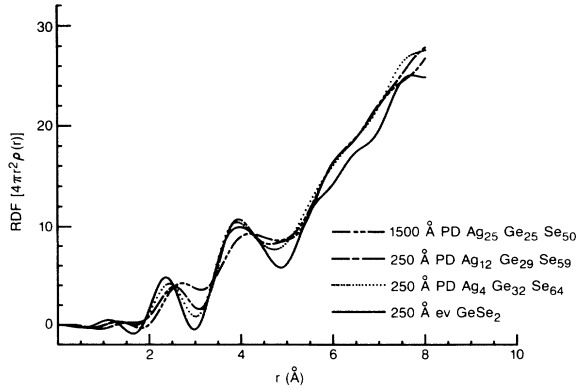


FIG. 4. Radial distribution functions (RDF's) of Ag-Ge-Se films made by photodiffusion of different amounts of Ag into evaporated $GeSe_2$ films.

TABLE II. Summary of the data-collection and analysis parameters used for the x-ray-scattering and RDF analysis performed in this work. See Sec. III B for a discussion of these parameters.

| | Sample | Incident angle $\phi$ (deg) | Density $\rho_0$ (g/cm$^2$) | Horizontal polarization | $K_{min}$ (Å$^{-1}$) |
|---|---|---|---|---|---|
| 2 | 250 Å pd $Ag_4Ge_{32}Se_{64}$ | 0.19 | 4.5 | 0.96 | 0.55 |
| 3 | 1500 Å pd $Ag_4Ge_{32}Se_{64}$ | 0.23 | 4.5 | 0.96 | 0.55 |
| 7 | 1500 Å sp $Ag_{10}Ge_{30}Se_{60}$ | 0.23 | 5.0 | 0.96 | 0.6 |
| 8[a] | sp $Ag_{10}Ge_{30}Se_{60}$ | | 5.0 | | 0.6 |
| 9 | MQ $Ag_{10}Ge_{36}Se_{54}$ | | 5.0 | | 0.6 |
| 4 | 250 Å pd $Ag_{12}Ge_{29}Se_{59}$ | 0.22 | 5.2 | 0.96 | 0.65 |
| 5 | 1500 Å pd $Ag_{25}Ge_{25}Se_{50}$ | 0.30 | 5.5 | 0.96 | 0.8 |

Data taken at 11 keV: $f'_{Ge}=-4.3$ electrons, $f''_{Ge}=0.5$ electrons; $f'_{Se}=-1.8$ electrons, $f''_{Se}=0.6$ electrons; $f'_{Ag}=-0.3$ electrons, $f''_{Ag}=2.5$ electrons

High-$k$ normalization range: 2.0–7.0 Å$^{-1}$

Fourier-transform data range: 0–6.2 Å$^{-1}$

Fourier-transform $\sigma$: 0.02 Å$^{-2}$

[a]Transmission x-ray measurement for sample 8:

Data taken at 25.4 keV: $f'_{Ge}=0.2$ electrons, $f''_{Ge}=0.9$ electrons; $f'_{Se}=0.2$ electrons, $f''_{Se}=1.2$ electrons; $f'_{Ag}=-4.9$ electrons, $f''_{Ag}=1.6$ electrons

High-$k$ normalization range: 10.0–11.0 Å$^{-1}$

Fourier-transform data range: 0–10.75 Å$^{-1}$

Fourier-transform $\sigma$: 0.02 Å$^{-1}$

rapidly. These trends show the modification of the original $a$-$GeSe_2$ structure with the addition of Ag.

The accuracy of the photodiffused RDF peak areas is estimated to be $\approx 8\%$ including the uncertainty in film density and normalization errors. In particular, for shorter-$k$-range data sets ($k_{max}<6.2$ Å) the larger $\sigma$ values ($\sigma^2\approx 0.02$) used with the Fourier transform (in the convergence factor) lead to a systematically larger peak area by $\approx 5\%$. In the final analysis here, the peak areas were reduced by this amount for the short-$k$-range, large-$\sigma$ data sets. The accuracy in peak position is estimated to be $\pm 0.01$ Å for bulk RDF's.[34] For the GIXS RDF analysis, the error may be somewhat larger because of large corrections to the data. In particular, larger (nonphysical) low-$r$ oscillations were usually obtained in the GIXS RDF's. In spite of this problem, the peak positions for bulk and films of $a$-$GeSe_2$ measured with bulk symmetric-Bragg and GIXS techniques, respectively, yielded the same first peak distances. This consistency implies that the data-analysis methods are reliable.

In Fig. 5 are the RDF's from the Ag-Ge-Se samples made with different methods: the 250-Å-thick photodiffused $Ag_{12}Ge_{29}Se_{59}$ film, the 1500-Å-thick sputtered $Ag_{10}Ge_{30}Se_{60}$ sample, and the bulk MQ $Ag_{10}Ge_{36}Se_{54}$ sample. While the overall appearances of these curves are quite similar, the MQ bulk $Ag_{10}Ge_{36}Se_{54}$ sample is slightly higher in density between 5 and 6 Å. The first-neighbor distance (see Table III) is slightly shorter for the 1500-Å-thick $Ag_{10}Ge_{30}Se_{60}$ sputtered sample (2.40 Å) than for the 250-Å-thick $Ag_{12}Ge_{29}Se_{59}$ film prepared by photodiffusion (2.47 Å). The peak areas are comparable, $\approx 3.0$ average atoms, for all three samples.

TABLE III. Summary of the RDF results for the different samples examined in this work.

| | Sample | Area (av. atoms) | Peak positions (Å) | | | |
|---|---|---|---|---|---|---|
| 2 | 250-Å pd $Ag_4Ge_{32}Se_{64}$ | 2.9 | 2.39 | 3.81 | 6.13[b] | 7.48 |
| 3 | 1500-Å pd $Ag_4Ge_{32}Se_{64}$ | 2.8[a] | 2.37 | 3.84 | 6.10[b] | 7.20[b] |
| 7 | 1500-Å sp $Ag_{10}Ge_{30}Se_{60}$ | 2.9 | 2.40 | 3.86 | 6.12 | 7.31 |
| 8 | bulk sp $Ag_{10}Ge_{30}Se_{60}$ | 3.0 | 2.40 | | | |
| 9 | bulk MQ $Ag_{10}Ge_{36}Se_{60}$ | 2.9 | 2.45 | 3.84 | 5.94 | 7.20 |
| 4 | 250-Å pd $Ag_{12}Ge_{29}Se_{59}$ | 3.0 | 2.47 | 3.86 | 6.11 | 7.10 |
| 5 | 1500-Å pd $Ag_{25}Ge_{25}Se_{50}$ | 3.3 | 2.62 | 3.97 | 6.15 | 7.08 |

[a]Large negative oscillations next to peak.

[b]Extremely broad peak.

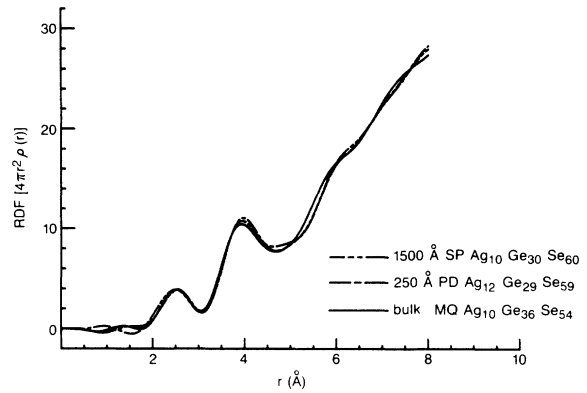


FIG. 5. Radial distributions functions (RDF's) of $a$-Ag-Ge-Se materials made by different methods. (Structure-dependent normalized scattering patterns in Fig. 3).

These results show than the local order of the photodiffused material and melt-quenched glass are quite similar, and not highly dependent on the method of preparation. The bond length for the sputtered sample is somewhat shorter, but the near-neighbor coordination is the same. Differences in composition (as well as uncertainty in composition) will also affect peak position, and may exaggerate differences.

X-ray-scattering data for a (13-$\mu$m) thick film of sputtered $Ag_{10}Ge_{30}Se_{60}$ film on Kapton, measured in a transmission geometry, were taken to compare to GIXS data of the same composition, and analyzed using the methods of Kortright.[36] These data were taken at 25.4 keV, and not the 11 keV of the GIXS data, so that the peak areas are somewhat different (due to differences in anomalous scattering factors). The first peak distance and area are 2.40 Å and 2.95 average atoms, respectively, compared to the 2.40 Å and 3.1 average atoms of the 1500-Å-thick film.

In summary, the GIXS results described thus far indicate the following.

(1) The short-range order in the 12% pd film appears identical to that in 10% MQ glass, within the sensitivity of the normal x-ray-diffraction techniques. The intermediate-range order may, however, be different. The short-range order in the sputtered sample appears to be slightly different.

(2) There is evidence for phase separation in the 12% and 25% Ag pd films. The presence of separation is uncertain in the 10% Ag materials, and seems unlikely in the 4% Ag pd films.

(3) The low-$k$ ($k=1$ Å$^{-1}$) peak disappears with increasing Ag concentration. This disappearance could be attributed to either of two (or both) possible causes. The first is a breakup of the Ge-Ge correlations associated with $a$-GeSe$_2$. This cause is inconsistent with a model for photodiffusion in which Ag diffuses only through isolated channels in $a$-GeSe$_2$, leaving the bulk of the material intact (described earlier).

A second possible cause, which is consistent with that model, is phase separation. In the photodiffusion model, the Ag diffuses through and reacts with Se-rich regions of the GeSe$_2$. Under such circumstances, one might expect separation into one phase with composition near $Ag_2Se$ or $Ag_8GeSe_6$ (the relevant compounds in the equilibrium phase diagram) and Ge-Se alloys. For example,

$$Ag_{0.10}Ge_{0.30}Se_{0.60} = 0.15(Ag_{0.67}Se_{0.33}) + 0.85(Ge_{0.35}Se_{0.65}) ,$$

or (7)

$$Ag_{0.10}Ge_{0.30}Se_{0.60} = 0.19(Ag_{0.53}Ge_{0.07}Se_{0.40}) + 0.81(Ge_{0.36}Se_{0.64})$$

and

$$Ag_{0.25}Ge_{0.25}Se_{0.50} = 0.38(Ag_{0.67}Se_{0.33}) + 0.62(Ge_{0.40}Se_{0.60}) ,$$

or (8)

$$Ag_{0.25}Ge_{0.25}Se_{0.50} = 0.47(Ag_{0.53}Ge_{0.07}Se_{0.40}) + 0.53(Ge_{0.42}Se_{0.58}) .$$

The Ge-Se compositions are all associated with glass formation, so that there is nothing inherently wrong with this picture. A difficulty, however, is that all these $a$-(Ge-Se) alloys show strong peaks in the region of $k=1$ Å$^{-1}$.[37] Thus, the disappearance of that peak with increasing Ag concentration would have to be ascribed to the fortuitous presence of a deep minimum in the scattered intensity of the Ag-containing phase near $k=1$ Å$^{-1}$. We cannot rule out that possibility. However, quasicrystalline modeling studies of $Ag_2Se$ and $Ag_8GeSe_6$ do not show such a minimum.

### D. Bulk Ag-Ge-Se differential anomalous scattering

DAS measurements and DDF analyses for the bulk MQ $Ag_{10}Ge_{36}Se_{54}$ sample were also made. Specifically, Ge, Se, and Ag $K$-edge DAS measurements were obtained for the MQ $Ag_{10}Ge_{36}Se_{54}$ sample. The x-ray energies and anomalous scattering factors are listed in Table IV. Ag $f'$ values somewhat more negative than theoretical Cromer and Liberman value ($-8.0$ instead of $-7.0$ electrons) at 14 eV below the edge significantly improved the Ag $K$-edge DDF in terms of the flatness of the low-$r$ region.

Figures 6–8 show the normalized data and DSF's for the MQ $Ag_{10}Se_{36}Se_{54}$ sample near the absorption edges of the three elements. We see from the difference curves that, as in the case of $a$-GeSe$_2$, the first peak is sensitive to changes in energy near the Ge $K$ edge, but not at the Se $K$ edge and probably not at the Ag $K$ edge, though the signal is quite noisy. While the scattering differences are relatively large at the Ge and Se $K$ edges, the changes in the signal at the Ag $K$ edge are extremely small. There is only 10 at. % Ag in the sample and the change in the anomalous scattering factor is only $\approx 3$ electrons for these energies, so we expect this result to be less reliable than the other two.

TABLE IV. Parameters used for the differential-distribution-function analysis. See Sec. III C for a discussion of these parameters.

| Sample | Energy | Normalization range (Å$^{-1}$) | Fourier-transform range (Å$^{-1}$) | Fourier transform $\sigma$ (Å$^{-2}$) |
|---|---|---|---|---|
| MQ $Ag_{10}Ge_{36}Se_{54}$ ($\rho_0$=5.0 g/cm$^3$) | Ge $K$ edge | 7.0–9.0 | 0–10.75 | 0.02 |
| | Se $K$ edge | 10.0–11.0 | 0–10.75 | 0.02 |
| | Ag $K$ edge | 10.0–11.0 | 0.5–10.75 | 0.02 |
| MQ $GeSe_2$ ($\rho_0$=4.2 g/cm$^2$) | Ge $K$ edge | 7.0–9.0 | 0.5–10.75 | 0.01 |
| | Se $K$ edge | 10.0–11.0 | 0.5–12.0 | 0.01 |

| | Energy (eV) | $f'_{Ge}$ | $f''_{Ge}$ | $f'_{Se}$ | $f''_{Se}$ (electrons) | $f'_{Ag}$ | $f''_{Ag}$ |
|---|---|---|---|---|---|---|---|
| Ge $K$ edge (11 104 eV) | 11 000 | −4.3 | 0.5 | −1.8 | 0.6 | −0.3 | 2.5 |
| | 11 090 | −7.0 | 0.5 | −1.9 | 0.6 | −0.3 | 2.5 |
| Se $K$ edge (12 568 eV) | 12 550 | −1.1 | 3.1 | −4.3 | 0.5 | −0.5 | 2.0 |
| | 12 645 | −1.1 | 3.1 | −7.5 | 0.5 | −0.5 | 2.0 |
| Ag $K$ edge (25 514 eV) | 25 400 | 0.2 | 0.9 | 0.2 | 1.1 | −4.9 | 0.5 |
| | 25 500 | 0.2 | 0.9 | 0.2 | 1.1 | −8.0 | 0.5 |

In Fig. 9 are shown the corresponding DDF's. We see that the first peak of the Ge $K$-edge DDF is dropping rapidly where the Ag $K$-edge DDF is peaked. In this region, the Se $K$-edge DDF does not reach the same deep minimum as does the Ge $K$-edge DDF, indicating that Ag is bonding to the Se, but not the Ge, as suggested by the XPS measurements discussed earlier. Further evidence in support of this conclusion is provided by the comparison of these DDF's to those of bulk $a$-$GeSe_2$ shown in Fig. 10. The Ge environment is very similar in the two glasses, but the Se environments are different. In particular, in the region beyond the first peak, in $a$-$GeSe_2$ there is also a deep minimum (as with the Ge DDF), but not in the Ag-Ge-Se glass.

Peak areas and positions are listed in Table V. In $Ag_{10}Ge_{36}Se_{54}$ the Ge, Se, and Ag nearest-neighbor distances are 2.39, 2.41, and 2.65 Å, respectively. Ge, Se, and Ag are approximately coordinated by 4, 2.9, and 3.9 atoms, respectively. The estimated accuracy of these results is 0.02 Å for peak positions and 8% for peak areas, including uncertainties in $f'_a$, average density, $\rho_0$, and normalization parameters.

### E. Ag EXAFS results

EXAFS measurements were made for the bulk MQ $Ag_{10}Ge_{36}Se_{54}$, the sputtered $Ag_{10}Ge_{30}Se_{60}$ film on Kapton, and the pd $Ag_7Ge_{31}Se_{62}$ samples. The Ag EXAFS (weighted by $k^3$ and windowed by a Gaussian-broadened square window at $k$ = 12 Å$^{-1}$) are shown in Fig. 11. We see from these curves the remarkable similarity of the Ag environment in these materials both in near-neighbor dis-

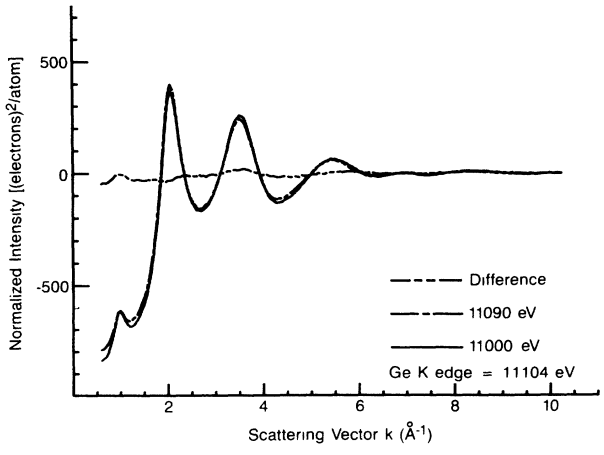


FIG. 6. Structure-dependent normalized Ge $K$-edge differential-anomalous-scattering (DAS) data and differential structure function (DSF) for bulk MQ $Ag_{10}Ge_{36}Se_{54}$ measured in symmetric Bragg geometry.

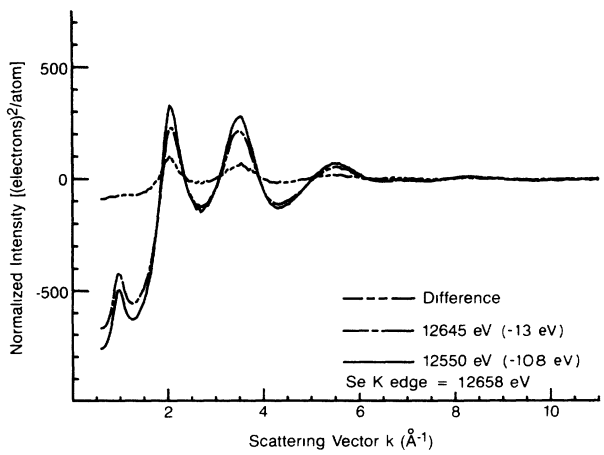


FIG. 7. Structure-dependent normalized Se $K$-edge differential-anomalous-scattering data and differential structure function for bulk MQ $Ag_{10}Ge_{36}Se_{54}$ measured in symmetric Bragg geometry.

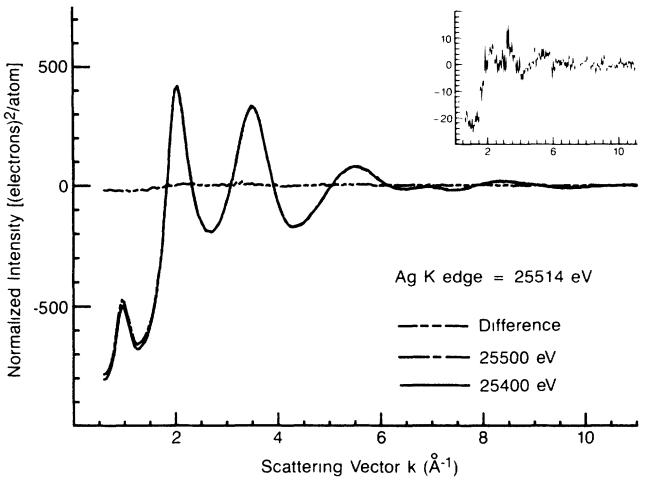


FIG. 8. Structure-dependent normalized Ag $K$-edge differential-anomalous-scattering data and differential structure function for bulk MQ $Ag_{10}Ge_{36}Se_{54}$ measured in symmetric Bragg geometry. The inset shows the Ag $K$-edge DSF on an expanded scale.

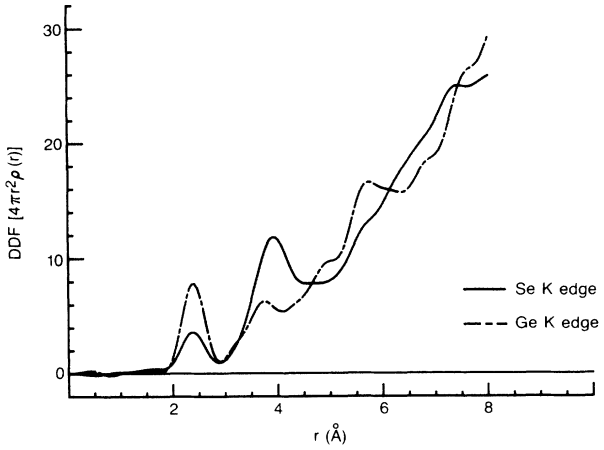


FIG. 10. Comparison of Se $K$-edge and Ge $K$-edge DDF's for bulk melt-quenched $GeSe_2$ (same as in Fig. 8). Analysis parameters are listed in Table IV and peak positions and first peak areas are listed in Table V.

tance (frequency) and coordination (amplitude). The sputtered sample appears to have a very slightly different frequency than the other two samples. These results are significant in that they indicate that the Ag near-neighbor environment is nearly independent of the method of sample preparation, although there is a slight difference for the sputtered sample.

Quantitative values for $R$, $N$, and $\sigma$, for different values of $E_0$ are given in Table VI, where the reference energy ($\Delta E_0$) occurs at the half-height of the edge jump of the absorption curve and we use a value of $E_0$ derived from Fourier-transform analysis. We have assumed that Se is the nearest neighbor of Ag, as indicated by XPS studies[10] and the DAS studies presented here. (Se and Ge have very similar backscattering amplitudes and phases, so that there is not much difference in the modeling results when either Se or Ge are assumed to be the nearest neighbor to Ag.) The difference (0.007 Å) between the near-neighbor distance of the pd film and the MQ glass is smaller than the combined precision of 0.02 Å. The distance for the sputtered film is somewhat shorter than for the other two glasses, with a small difference of 0.024 Å compared to the MQ glass. As seen in Table VI, values for the coordination $N$ are quite similar. The absolute values of $N$ are not considerable reliable since they are based on theoretical analysis parameters, rather than on empirical (by comparison to a standard component) ones and also because of reasons discussed at the end of this section.

Figure 12 shows the Ag EXAFS for the pd film compared to crystalline $Ag_2Se$. Both the frequencies and the amplitudes of the EXAFS are quite different. In particular, the amplitude of $Ag_2Se$ EXAFS is less than that for the pd film EXAFS. This smaller amplitude may reflect either a lower coordination or the interference due to a

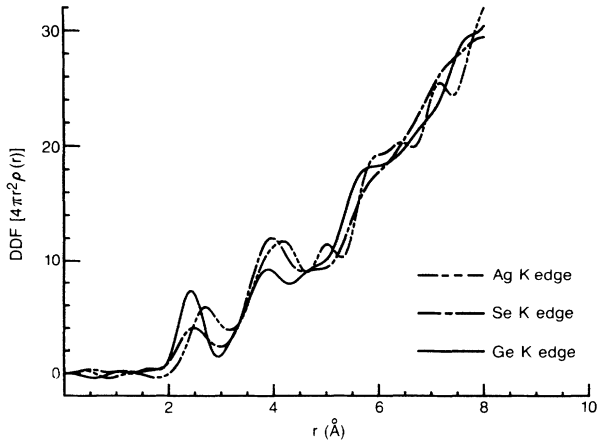


FIG. 9. Differential distribution functions calculated from Ge, Se, and Ag $K$-edge DAS measurements of Figs. 6–8.

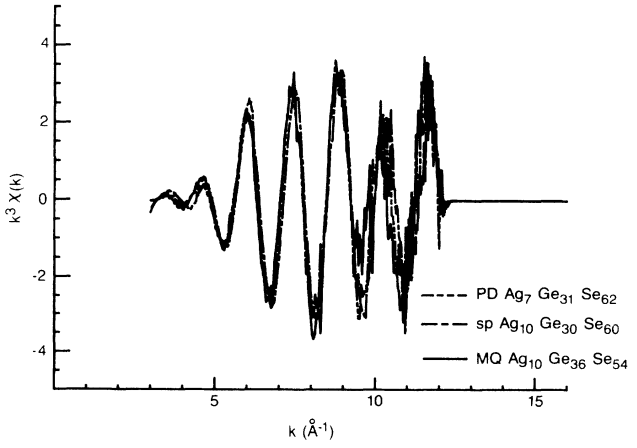


FIG. 11. Comparison of Ag $K$-edge EXAFS, $k^3\chi(k)$, for melt-quenched $Ag_{10}Ge_{36}Se_{54}$, sputtered $Ag_{10}Ge_{30}Se_{60}$, and photodiffused $Ag_7Ge_{31}Se_{62}$.

TABLE V. Summary of the differential-distribution-function analysis. These results are discussed in Sec. IV D.

| Sample | Energy | Nearest neighbors (at. % $n$-$n$; Ag coordination) | Area (av. atoms) | Peak positions (Å) |
|---|---|---|---|---|
| MQ $Ag_{10}Ge_{36}Se_{54}$ | Ge $K$ edge | (32 Ge, 68 Se; $Q_{Ag}=3$) | 4.2 | |
| | | (32 Ge, 68 Se; $Q_{Ag}=4$) | 4.2 | 2.39, 3.81, 4.64, 5.67, 6.68. 7.59 |
| | Se $K$ edge | (0 Se, 23 Ag; $Q_{Ag}=3$) | 2.9 | |
| | | (0 Se, 29 Ag; $Q_{Ag}=4$) | 2.9 | 2.41, 3.88, 5.85. 7.19 |
| | Ag $K$ edge | (100 Se) | 3.9 | 2.65, 4.00, 4.94, 5.58, 6.30, 7.10 |
| MQ $GeSe_2$ | Ge $K$ edge | (100 Se) | 4.2 | 2.37, 3.68, 4.89, 5.65, 6.79, 7.53 |
| | Se $K$ edge | (100 Ge) | 2.0 | 2.35, 3.88, 5.65, 6.29, 6.71, 7.30 |

range of near-neighbor distances, as found in all of the crystalline modifications of $Ag_2Se$.

The shortest $c$-$Ag_2Se$ distance is $\approx 0.1$ Å longer than any of the distances found in the glasses. This difference suggests a difference in the type of bond formed by Ag in the two materials. That is, the bonding in the amorphous material is significantly more covalent than that in the crystalline compounds. This points is utilized later in the context of a local-bonding model proposed here for these glasses.

In summary of the Ag EXAFS results, we have observed trend in the Ag nearest-neighbor distance in the glasses which show that the environment of the Ag in the pd film is quite similar to that of the MQ glass, and that these distances are slightly longer than those of the amorphous sputtered film. A similar trend was observed in the RDF's, although the RDF is more sensitive to exact composition. The differences in distance, however, are small. The Ag coordinations in the glasses are about the same. Covalent bonding of Ag in all of the glasses is indicated by shorter distances than those of crystalline $Ag_2Se$.

It should be noted, however, that absolute distances and coordination numbers were not determined in this EXAFS work. Indeed, there is a marked difference between the Ag coordination number ($\approx 4$) obtained from the DAS study of the MQ glass and that ($\approx 1$) obtained for that sample from EXAFS. As stated above, one reason for this is that a suitable standard is not available, so that calculated backscattering amplitudes and phase shifts were utilized. Often the coordination numbers obtained under such circumstances are too small by 30–50 %.

A second large contribution to the discrepancy is the asymmetric shape of the distribution of atoms bonded to Ag, as shown in the Ag DDF of Fig. 9. Under such circumstances, EXAFS analyzed in the standard plane-wave approximation can yield coordination numbers which are less than 25% of the value provided by DAS techniques, as discussed by Kortright and Bienenstock.[38]

TABLE VI. EXAFS results where $\Delta E_0$ is referenced to at the half-height of the edge jump of the absorption curve, $R$ is the first-neighbor distance, $N$ is the first-neighbor coordination, and $\sigma^2$ is the Gaussian disorder associated with the first-neighbor shell.

| Sample | $\Delta E_0$ (eV) | $R$ (Å) | $N$ | $\sigma^2$ (Å$^{-2}$) |
|---|---|---|---|---|
| MQ $Ag_{10}Ge_{36}Se_{54}$ | 2 | 2.52 | 0.8 | 0.0044 |
| sp $Ag_{10}Ge_{30}Se_{60}$ | 2 | 2.49 | 0.8 | 0.0039 |
| pd $Ag_7Ge_{31}Se_{62}$ | 7 | 2.51 | 1.2 | 0.0078 |

## V. STRUCTURAL INTERPRETATION

In this section we present a local (nearest-neighbor) structural model for the pd Ag-$GeSe_2$ materials (and other $a$-Ag-Ge-Se glasses) and compare the calculated RDF and DDF peak positions and areas to the measured results.

Construction of the model begins with the physical situation associated with the photodiffusion phenomenon. That is, Ag is introduced into $a$-$GeSe_2$. In the pure $GeSe_2$, Ge is fourfold coordinated by Se and Se is twofold coordinated by Ge. Considered here is the situation in which two Ag atoms are introduced into such a system.

We assume that Kastner's picture[12] of Ag in amorphous chalcogenides is valid. In this picture, Ag forms one covalent bond (with its 5$s$ electron) and up to three coordination (or dative) bonds with Se lone-pair electrons to obtain a maximum coordination number of 4. This picture is consistent with the evidence presented here that the Ag bonds to the Se in these materials.

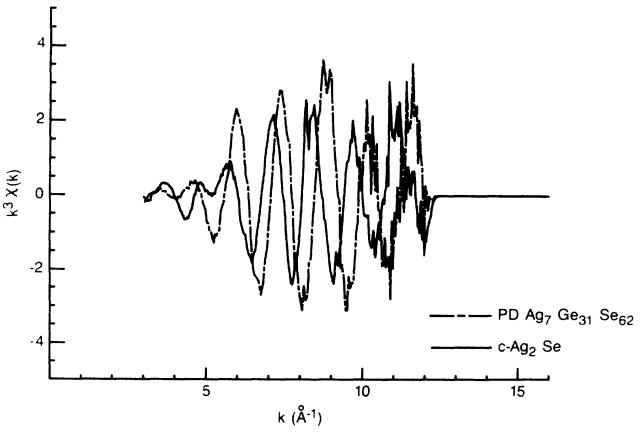


FIG. 12. Ag $K$-edge EXAFS, $k^3\chi(k)$, for photodiffused $Ag_7Ge_{31}Se_{62}$ compared to crystalline $Ag_2Se$.

In order for a Se atom to bond covalently with a Ag, a preexisting Se—Ge bond must be broken. Thus, for counting purposes, each Ag yields a dangling Ge bond. Therefore, we assume that each pair of Ag atoms introduced into the system yields one Ge—Ge bond.

This simple picture must be generalized, however, because the samples studied here have Ag:Ge:Se ratios which cannot be described as mixtures of Ag with $GeSe_2$. In the more general form, it is assumed that Ge forms four covalent bonds and Se two covalent bonds, with a preference for unlike-atom bonds. In the materials studied here (Ge rich), it is necessary to postulate that Ge—Ge bonds are formed, particularly since some of the two covalent bonds per Se are tied to Ag. There are no Ag—Ag, Se—Se, or Ag—Ge bonds in the model.

For that portion of the Ag-Ge-Se system for which $X_{Ag} < X_{Se}$ and $2X_{Ge} > X_{Se}$ (where $X_{Ag}$ is the mole fraction of Ag, etc.), we can count bonds to determine coordination numbers. For example, to determine the number of Se neighbors for each Ge atom, we note that the number of Ge—Se bonds ($N_{GeSe}$) is given by the coordination number of Se (2), the number of Se atoms ($N_{Se}$), the covalent bonds on a Ag atom ($Q_{Ag}$, which is assumed to be 1 here), and the number of Ag atoms ($N_{Ag}$) by the simple relationship

$$N_{GeSe} = 2N_{Se} - Q_{Ag}N_{Ag} \ . \tag{9}$$

Expressing the number of Se and Ag atoms in terms of the total number of atoms, $N_{tot}$, and the atomic fraction, we obtain

$$X_{Ge}C_{GeSe}N_{tot} = (2X_{Se} - Q_{Ag}X_{Ag})N_{tot} \ , \tag{10}$$

or

$$C_{GeSe} = 2\frac{X_{Se}}{X_{Ge}} - Q_{Ag}\frac{X_{Ag}}{X_{Ge}} \ , \tag{11}$$

where $C_{GeSe}$ is the coordination of Se around Ge. Using this procedure, we can derive a set of equations that describes the average coordination around each type of atom. The resulting relationships are
sulting relationships are

$$C_{GeGe} = 4 - 2\frac{X_{Se}}{X_{Ge}} + Q_{Ag}\frac{X_{Ag}}{X_{Ge}} \ , \tag{12a}$$

$$C_{GeSe} = 2\frac{X_{Se}}{X_{Ge}} - Q_{Ag}\frac{X_{Ag}}{X_{Ge}} = \frac{X_{Se}}{X_{Ge}}C_{SeGe} \ , \tag{12b}$$

$$C_{GeAg} = 0 = C_{AgGe} \ , \tag{12c}$$

$$C_{SeSe} = 0 \ , \tag{12d}$$

$$C_{SeAg} = \frac{X_{Ag}}{X_{Se}}Q^*_{Ag} = \frac{X_{Ag}}{X_{Se}}C_{AgSe} \ , \tag{12e}$$

$$C_{AgAg} = 0 \ . \tag{12f}$$

Here, $Q^*_{Ag}$ is the total coordination of a Ag atom, i.e., it includes neighbors which are both covalently and coordinately bonded. For the fourfold total coordination of Ag, 31 at. % Ag can be added to $a$-$GeSe_2$, at which point all of the Se lone pairs are bonded to Ag. For threefold total coordination of Ag, a Ag concentration of 40 at. % can be reached. It is interesting to note that the crystalline compound in the Ag-Ge-Se system, $Ag_8GeSe_6$, has a composition such that $C_{GeGe} = 0$.

This model can be used with the RDF's to determine the remaining unknown coordination number, $C_{AgSe}$, by counting bonds and calculating the first peak areas. The first peak distances can be calculated assuming that bond lengths are comparable to those found in materials such as $a$-$GeSe_2$, $a$-Ge, and $c$-$Ag_2Se$ or $c$-$Ag_8GeSe_6$. In addition, the Ag-Se distance, for which there is a large range of distances in crystalline compounds (2.45–2.86 Å), is treated as an unknown. In principle, this length can be determined from the position of the first peak.

Using the preceding rules and our earlier RDF analysis methods, the RDF first peak area, which is the average number of atoms around an average central atom, is given by

$$\frac{2X_{Ge}C_{GeSe}f_{Ge}f_{Se} + X_{Ge}C_{GeGe}f^2_{Ge} + 2X_{Ag}C_{AgSe}f_{Ag}f_{Se}}{X_{Ge}f^2_{Ge} + X_{Se}f^2_{Se} + X_{Ag}f^2_{Ag}} \ , \tag{13}$$

where $f_{Ge}$, the average scattering factor, is given by

$$f_{Ge} = \langle f_{Ge}(k=0)\rangle = [(Z_{Ge} + f'_{Ge})^2 + (f''_{Ge})^2]^{1/2} \ , \tag{14}$$

where $Z_{Ge}$ is the atomic number of Ge, and $f'_{Ge}$ and $f''_{Ge}$ are the anomalous scattering factors. The expressions for $f_{Se}$ and $f_{Ag}$ are analogous.

Similarly, the first peak distance is the average bond length of the first neighbor shell and is given by

$$\frac{2X_{Ge}C_{GeSe}R_{GeSe} + X_{Ge}C_{GeGe}R_{GeGe} + 2X_{Ag}C_{AgSe}R_{AgSe}}{2X_{Ge}C_{GeSe} + X_{Ge}C_{GeGe} + 2X_{Ag}C_{AgSe}} \ , \tag{15}$$

where $R_{GeSe}$, $R_{GeGe}$, and $R_{AgSe}$ are the average first-neighbor distances.

Calculations of the first peak areas for the different Ag-Ge-Se compositions are listed in Table VII. In these calculations, we have used the RDF peak area obtained from the measurements and calculated the unknown Ag coordination, $Q^*_{Ag}$, using Eq. (11). The Ag coordinations

TABLE VII. Estimate of the first-neighbor Ag coordination of Se. These results are derived using Eq. (13) and are discussed in Sec. V.

| Sample | Thickness (Å) | RDF area (atoms) | Ag coord. (atoms) |
|---|---|---|---|
| pd $Ag_4Ge_{32}Se_{64}$ | 1500 | 2.8 | 3.7 |
| | 250 | 2.9 | 4.1 |
| pd $Ag_{12}Ge_{29}Se_{59}$ | 250 | 3.1 | 3.5 |
| pd $Ag_{25}Ge_{25}Se_{50}$ | 1500 | 3.5 | 3.5 |
| sp $Ag_{10}Ge_{30}Se_{60}$ | 1500 | 3.2 | 3.9 |
| | bulk | 3.0 | 3.7 |
| MQ $Ag_{10}Ge_{36}Se_{54}$ | bulk | 3.1 | 3.7 |

TABLE VIII. Estimated Ag—Se bond distances derived using Eq. (15). These results are discussed in Sec. V.

| Sample | Thickness (Å) | Meas. RDF Dist. (Å) | Ag-Se Dist.[a] (Å) | Ag-Se Dist.[b] ($N_{Ag}=4$) (Å) |
|---|---|---|---|---|
| pd $Ag_4Ge_{32}Se_{64}$ | 1500 | 2.37 | <2.45 | <2.45 |
| | 250 | 2.39 | 2.48 | 2.48 |
| pd $Ag_{12}Ge_{29}Se_{59}$ | 250 | 2.47 | 2.62 | 2.66 |
| pd $Ag_{25}Ge_{25}Se_{50}$ | 1500 | 2.62 | 2.76 | 2.74 |
| sp $Ag_{10}Ge_{30}Se_{60}$ | 1500 | 2.40 | 2.45 | <2.45 |
| | bulk | 2.40 | 2.45 | <2.45 |
| MQ $Ag_{10}Ge_{36}Se_{54}$ | bulk | 2.46 | 2.60 | 2.59 |

[a]Calculation of Ag-Se distance, assuming Ag coordination obtained from RDF area with model (see Table VII).
[b]Calculation of Ag-Se distance, assuming a coordination of 4.

TABLE IX. Comparison of the MO $Ag_{10}Ge_{36}Se_{54}$ DDF areas and the postulated structural model (Ge—Ge model bond length, 2.45 Å; Ge-Se model bond length, 2.36 Å.)

| | | DDF area (av. atoms) | Model DDF area (av. atoms) |
|---|---|---|---|
| Ge $K$ edge | $Q_{Ag}=3$ | 4.2 | 3.9 |
| | $Q_{Ag}=4$ | 4.2 | 3.9 |
| Se $K$ edge | $Q_{Ag}=3$ | 2.9 | 2.8 |
| | $Q_{Ag}=4$ | 2.9 | 3.0 |
| Ag $K$ edge | $Q_{Ag}=3$ | 3.9 | 3.0 |
| | $Q_{Ag}=4$ | | 4.0 |

calculated from the RDF peak areas range from ≈3.5 to 4.1 average (Se) atoms. There is potentially large error associated with this result since the Ag comprises only a small percentage of the total peak area. If we assume that the RDF area can vary by 8%, then for the 4-at. % Ag sample, the measured coordination may range from ≈2 to ≈5 atoms, while for the 25-at. % Ag sample, the range is only ≈3 to ≈4 atoms. In spite of these difficulties, the Ag coordination appears to be very similar in all of the amorphous Ag-Ge-Se glasses. This result agrees well with the local Ag bonding proposed by Kastner. There is a trend to lower Ag coordination with higher Ag concentration, but a definitive result would require more accurate measurements.

With the first peak distance and Ag coordination obtained from the RDF's, we calculate the Ag—Se bond length using Eq. (12). These distances along with the assumed Ge—Ge and Ge—Se bond lengths are listed in Table VIII. In addition, Table VIII shows the Ag—Se bond length calculated assuming a Ag coordination of 4. The Ag—Se distances calculated from the RDF peak position fall into a broad range of distances, 2.45–2.74 Å, which is consistent with the broad range of Ag—Se distances found in the crystalline compounds $Ag_8GeSe_6$ and $Ag_2Se$. The Pauling Ag—Se covalent-bond distance is 2.66 Å. In the context of the model, these results lead to the conclusion that all of these materials have covalent Ag—Se bonds, in spite of the fact that Ag photodiffuses ionically through $a$-$GeSe_2$.

For the photodiffused Ag-Ge-Se samples, there is a trend to slightly longer Ag—Se bond length with increasing Ag concentration. The sputtered $Ag_{10}Ge_{36}Se_{54}$ sample have very short Ag—Se bond lengths, while the melt-quenched sample $Ag_{10}Ge_{36}Se_{54}$ has bond lengths similar to the photodiffused samples of similar Ag concentration. The trends observed here are also subject to the large errors as for Ag coordinations and are not considered to be necessarily valid. It should be possible to prove the validity of these observed compositional trends with the higher-quality data obtainable with the advances in synchrotron radiation presently becoming available.

The DDF analysis then provides the means of testing the model with the one sample for which such data are available, $Ag_{10}Ge_{36}Se_{54}$. A similar analysis can be used to interpret the DDF results. In particular, the general expression for the DDF first peak area for a three-component system, $a,b,c$ (at the $K$-absorption edge of element $a$), is given by

$$\int \Gamma\, dr = \frac{(C_{aa}-V\rho_{a,0})(2Z_a+f'_{a1}+f'_{a2})+2(C_{ab}-V_{\rho b,0})(Z_b-f'_{b1})+2(C_{ac}-V\rho_{c,0})(Z_c+f'_{c1})+V_\rho}{F_{aa}(2Z_a+f'_{a1}+f'_{a2})+F_{ab}2(Z_b+f'_{b1})+F_{ac}2(Z_{zc}+f'_{c1})}\,, \tag{16}$$

where $\Gamma$ is the DDF and $Z_a$, $Z_b$, and $Z_c$ are the atomic numbers of elements $a$, $b$, and $c$; $f'_{a1}$, $f'_{a2}$, $f'_{b1}$, and $f'_{c1}$ are the real anomalous scattering factor at energies 1 and 2; $C_{aa}$, $C_{ab}$, and $C_{ac}$ are the coordinations of $a$ around $a$, $b$ around $a$, and $c$ around $a$; $V$ is the volume of the first-neighbor shell; $\rho_{a,0}$, $\rho_{b,0}$, and $\rho_{c,0}$ are the average densities of elements $a$, $b$, and $c$; and $F_{aa}$ is the estimated fraction of $a$ around $a$, $F_{ab}$ is the estimated fraction of $b$ around $a$, and $F_{ac}$ is the estimated fraction of $c$ around $a$. This equation is obtained by the integration of Eq. (7) over the first-neighbor shell. This expression is simplified for the including the assumed chemical order (e.g., $C_{AgGe}=0$, $F_{AgGe}=0$).

A comparison of the DDF areas of $Ag_{10}Ge_{36}Se_{54}$ and the model, using $Q^*_{Ag}=3.7$, are listed in Table IX. Good agreement is obtained for DDF's obtained at all three edges. This result indicates that the basic short-range structural features of the model are valid.

The DDF first peak distance, $D$, for a three-component system can be calculated according to (near the $K$-absorption edge of element $a$)

$$D=\frac{(2Z_a+f'_{a1}+f'_{a2})C_{aa}R_{aa}+2(Z_b+f'_{b1})C_{ab}R_{ab}+2(Z_c+f'_{c1})C_{ac}R_{ac}}{(2Z_a+f'_{a1}+f'_{a2})C_{aa}+2(Z_b+f'_{b1})C_{ab}+2(Z_c+f'_{c1})C_{ac}}\ , \tag{17}$$

where $R_{aa}$, $R_{ab}$, and $R_{ac}$ are the $a$—$a$, $a$—$b$, and $a$—$c$ bond lengths.

The Ag—Se bond distance obtained from the Ag-edge DDF of MQ $Ag_{10}Ge_{36}Se_{54}$ is 2.65 Å, about 0.05 Å longer than that deduced from the RDF. The EXAFS analysis yields a shorter Ag—Se bond length, 2.49–2.52 Å (shorter than the RDF results by $\approx 0.1$ Å). Also, the variations in bond length with sample are much smaller than those suggested by the RDF results. We expect the relative errors in the RDF results to be much larger than for the EXAFS. Also, we note that the EXAFS technique generally picks out the shortest distance, particularly for asymmetric distributions.[39] Given the accuracy of these techniques and the smallness of the variations, we cannot tell if there are subtle trends to the bond lengths with composition. Overall, we conclude that all of these measurements yield results consistent with each other.

The picture which emerges for the pd material is schematically shown in Fig. 13. In the figure is shown $a$-$GeSe_2$, in which all of the Ge are fourfold coordinated by Se and all of the Se are twofold coordinated by Ge. (We are not concerned about intermediate-range order in this model, and intend to convey only that Ge and Se bonding requirements are properly satisfied in this schematic.) With the addition of two Ag atoms, two Ge—Se bonds are broken and each Ag atom forms a covalent bond with Se. This leaves two unbonded Ge atoms which can form a Ge—Ge bond. Thus, the addition of a pair of Ag atoms results in a Ge—Ge bond. Ag also forms coordination bonds with any available Se lone-pair atoms. A detailed model incorporating these concepts would require large structural rearrangements during the photodiffusion of Ag, as suggested by the x-ray-scattering data.

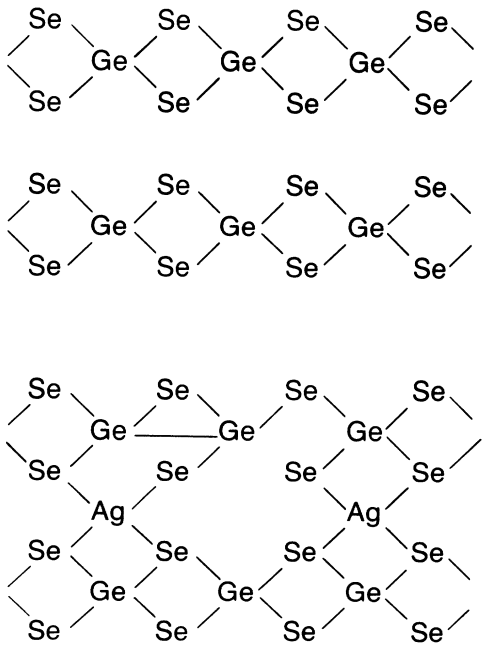


FIG. 13. Schematic of $GeSe_2$ before Ag photodiffusion and after Ag photodiffusion.

This picture agrees with the RDF and DDF results observed for these materials. In addition, it can be used to explain the disappearance of the low-$k$ peak with the addition of Ag. Ge—Ge bonds disrupt the chemical order of the system and put Ge atoms at distances (specifically nearest neighbor) which will reduce the strength of the low-$k$ peak. In addition, with an overall disordering of the system, we would expect that larger-distance interferences (farther than nearest neighbor) also would decrease the intensity of the peak.

Finally, these results are consistent with the changes in the optical spectra,[11] in which it was observed that the excitation of the Se lone-pair electrons could be resolved for $a$-$GeSe_2$, but not samples into which 10 at. % Ag had been photodiffused. The rearrangements described here, in which Se lone-pair electrons are tied up in bonding with Ag photodiffusion, explains these results.

It should be noted that the model addresses the short-range, but not the intermediate-range, order. It is, in fact, consistent with either a homogeneous distribution of Ag atoms or phase separation of the type discussed in Sec. IV. C.

## VI. CONCLUSIONS

These results demonstrate the power of the GIXS technique in the study of thin amorphous films (ranging from 250 Å to bulk thicknesses). The critical parameters of the GIXS technique are a high incident-beam intensity and collimation (high brillance, photons/s m$^2$ mrad$^2$—0.1% bandwidth) to provide both a measurable scattered signal from such a small amount of weakly scattering material as well as depth sensitivity. We have been able to determine the normalized (structure dependent) scattered intensity as a function of $k$, so that data sets from different samples and even measurements using different scattering geometries (e.g., symmetric Bragg scattering from bulk samples) can be compared. Peak count rates for $a$-$GeSe_2$ were approximately 1 count/s per Å thickness of film at SSRL on wiggler BL-4 (8 poles, 18 kG) using a focusing mirror, with the SPEAR storage ring operating at 3 GeV and $\approx 50$ mA current.

High-quality RDF's were obtained from the Fourier transform of the $a$-Ag-Ge-Se data and agreed well with RDF's obtained from bulk samples measured in the standard symmetric Bragg geometry. The resolution of the RDF was limited by the somewhat short $k$ range of 6.2 Å$^{-1}$ because of the large polarization necessary with the sample surface oriented nearly horizontally. As discussed, this orientation was used to maximize both the amount of beam striking the sample as well as the depth sensitivity of the measurement. We expect that the next

generation of synchrotron-radiation sources will eliminate this requirement and that highly accurate studies of amorphous thin films will be possible.

From these measurements, we have determined that the local atomic structure of Ag-$GeSe_2$ films satisfies a model derived from the Kastner picture in that (1) the Se—Ag bonding is consistent with the formation of dative bonds, (2) one Se—Ag covalent bond is formed for each Ag atom added to the system up to a critical concentration, and (3) that Ge—Ge bonds are created as Ag is added and significantly affect the intermediate-range order in this system. The model can be sustained to an Ag concentration of 31 at. % if Ag is fourfold coordinated by Se, or 40 at. % if the Ag is threefold coordinated.

The short-range model presented here is consistent with both a homogeneous Ag distribution or phase separation into a Ag-containing phase like $Ag_2Se$ or $Ag_8GeSe_6$ (the crystalline compounds in the system) plus a Ge-Se alloy. That portion of the small-angle-scattering (SAXS) curve which was measured with the GIXS indicates the presence of phase separation for the 25 at. % Ag and probably, for the 12 at. % Ag pd samples, but not not for the 4 at. %. The fact that the SAXS is observable at relatively high angles indicates that the separation must be on a very fine scale. Such fine-scale separation would limit the Ge-Ge correlations which account for the low-$k$ peak in the scattering from the amorphous Ge-Se alloys and account for the disappearance of the peak as the Ag concentration increases.

## ACKNOWLEDGMENTS

We would like to thank. J. DeNeufville for providing some of the samples used in these experiments and F. Lytle for the use of his fluorescence EXAFS detector. This work was initiated with partial support from National Science Foundation Grant No. DMR-82-05401. Subsequently, two of us (A.F.C. and A.I.B.) were supported by the U.S. Department of Energy through SSRL. The work reported herein was partially done at SSRL, which is supported by the U.S. Department of Energy (Office of Basic Energy Sciences) and by the National Institutes of Health (Biotechnology Resource Program, Division of Research Resources).

*Present address: Hewlett-Packard Laboratories, 3500 Deer Creek Rd., Palo Alto, CA 94304-1317.

[1]An extensive overview of the photodiffused Ag-$GeSe_2$ and related materials studies is given in *Proceedings of the Symposium on Inorganic Resist Systems,* edited by D. A. Doane and A. H. Heller (Electrochemical Society, Pennington, NJ, 1982), pp. 82–89.

[2]A. Wagner and D. Barr, in Ref. 1, p. 281.

[3]*CRC Handbook of Chemistry and Physics, 62nd. ed.* edited by R. C. Weast and M. J. Astle (Chemical Rubber Co., Boca Raton, FL, 1981).

[4]W. C. Marra, P. Eisenberger, and A. Y. Cho, J. Appl. Phys. **50**, 6927 (1979).

[5]W. C. Marra, P. H. Fuoss, and P. Eisenberger, Phys. Rev. Lett. **49**, 1169 (1982).

[6]P. H. Fuoss and A. Fischer-Colbrie, Phys. Rev. B **38**, 1875 (1988).

[7]P. Tronc, M. Bensoussan, A. Brenac, and C. Sebanne, Phys. Rev. B **8**, 5947 (1973).

[8]J. C. Phillips, J. Non-Cryst. Solids **43**, 37 (1981); in Ref. 1, p. 147.

[9]P. Boolchand, J. Grothaus, W. J. Besser, and P. Suranyi, Phys. Rev. B **25**, 2975 (1982).

[10]S. Zembetsu, Appl. Phys. Lett. **39**, 969 (1981).

[11]D. E. Aspnes, J. C. Phillips, K. L. Tai, and P. M. Bridenbaugh, Phys. Rev. B **23**, 816 (1981).

[12]M. A. Kastner, Philos. Mag. B **37**, 127 (1978).

[13]S. H. Hunter, A. Bienenstock, and T. M. Hayes, in *Proceedings of the 7th International Conference on Amorphous and Liquid Semiconductors, Edinburg, 1977,* edited by W. E. Spear, p. 78.

[14]S. Laderman, A. Bienenstock, and K. S. Liang, Sol. Energy Mater. **8**, 15 (1982).

[15]A. Fischer-Colbrie, Ph.D. thesis, Stanford University, 1986; available as Stanford Synchrotron Radiation Report No. 86/05, 1986 (unpublished).

[16]P. H. Fuoss and A. Fischer-Colbrie (unpublished).

[17]P. H. Fuoss, Ph.D. thesis, Stanford University, 1980; available as Stanford Synchrotron Radiation Laboratory Report 80/06, 1980 (unpublished).

[18]B. E. Warren, *X-Ray Diffraction* (Addison-Wesley, Reading, MA, 1973).

[19]D. T. Cromer and J. Mann, Acta Crystallogr. Sect. A **24**, 321 (1968).

[20]H. H. M. Balyuzi, Acta Crystallogr. Sect. A **31**, 600 (1975).

[21]D. T. Cromer and D. Liberman, J. Chem. Phys. **53**, 1891 (1970).

[22]H. W. Winick, in *Synchrotron Radiation Research,* edited by H. Winick and S. Doniach (Plenum, New York, 1980), p. 11; J. Schwinger, Phys. Rev. **75**, 1912 (1949).

[23]E. A. Stern and S. M. Heald, Rev. Sci. Instrum. **50**, 1579 (1979).

[24]B. K. Teo and P. A. Lee, J. Am. Chem. Soc. **101**, 2815 (1979).

[25]B. Lengeler and P. Eisenberger, Phys. Rev. B **21**, 4507 (1980).

[26]P. A. Lee, P. H. Citrin, P. Eisenberger, and B. M. Kincaid, Rev. Mod. Phys. **53**, 769 (1981).

[27]P. H. Fuoss, P. Eisenberger, W. K. Warburton, and A. Bienenstock, Phys. Rev. Lett. **46**, 1537 (1981).

[28]P. Rahlfs, Z. Phys. Chem. B **31**, 157 (1936).

[29]R. de Ridder, J. de Sitter, and S. Amelinckx, Phys. Status Solidi A **23**, 615 (1974).

[30]T. Sakuma, K. Iida, K. Honma, and H. Okazaki, J. Phys. Soc. Jon. **43**, 538 (1977).

[31]Z. G. Pinsker, C. Ching-liang, R. M. Imamov, and E. L. Lapidus, Kristallografiya **10**, 275 (1965) [Sov. Phys.—Crystallogr. **10**, 225 (1965)].

[32]G. A. Wiegers, Am. Mineral. **56**, 1882 (1971).

[33]D. Carre, R. Ollirault-Fichet, and J. Flahaut, Acta Crystallogr. Sect. B **36**, 245 (1980).

[34]K. F. Ludwig, Jr., W. K. Warburton, L. Wilson, and A. I. Bienenstock, J. Chem. Phys. **87**, 604 (1987).

[35]V. G. Dittmar and H. Shafer, Acta Crystallogr. Sect. B **32**,

245 (1980).
[36]J.B. Kortright, Ph.D. thesis, Stanford University, 1985, available as Stanford Synchrotron Radiation Laboratory Report No. 84/05, 1984 (unpublished).
[37]A. Bienenstock, F. Mortyn, S. Narasimhan, and S. C. Rowland, in *Frontiers of Materials Science: Distinguished Lectures,* edited by L. Murr and C. Stein (Dekker, New York, 1976), p. 1.
[38]J. B. Kortright and A. Bienenstock, Phys. Rev. B **37**, 2979 (1988).
[39]J. B. Kortright, W. K. Warburton, and A. I. Bienenstock, in *EXAFS and Near Edge Structure,* Vol. 27 of *Springer Series in Solid State Physics,* edited by A. Bianconi, L. Incoccia, and S. Stipcich (Springer, New York, 1983), p. 362.